

Deterministic actin waves as generators of cell polarization cues

Luiza Stankevics^{a,1}, Nicolas Ecker^{b,c,1}, Emmanuel Terriac^a, Paolo Maiuri^d, Rouven Schoppmeyer^e, Pablo Vargas^{f,g}, Ana-Maria Lennon-Duménil^f, Matthieu Piel^{h,i}, Bin Qu^d, Markus Hoth^e, Karsten Kruse^{b,c,j}, and Franziska Lautenschläger^{a,k,2}

^aBio Interfaces, Leibniz Institute for New Materials, 66123 Saarbrücken, Germany; ^bDepartment of Biochemistry, University of Geneva, 1211 Geneva, Switzerland; ^cDepartment of Theoretical Physics, University of Geneva, 1211 Geneva, Switzerland; ^dInternational Foundations of Medicine (IFOM), The Fondazione Italiana per la Ricerca sul Cancro (FIRC) Institute of Molecular Oncology, 20139 Milano, Italy; ^eDepartment of Biophysics, Center for Integrative Physiology and Molecular Medicine, School of Medicine, Saarland University, 66421 Homburg, Germany; ^fINSERM U932, Institut Curie, 75005 Paris, France; ^gCNRS UMR144, Institut Curie, 75005 Paris, France; ^hInstitut Curie, CNRS, UMR 144, Université Paris Sciences et Lettres (PSL) Research University, 75005 Paris, France; ⁱInstitut Pierre-Gilles de Gennes, PSL Research University, 75005 Paris, France; ^jNational Center for Competence in Research Chemical Biology, University of Geneva, 1211 Geneva, Switzerland; and ^kDepartment of Natural Sciences, Saarland University, 66123 Saarbrücken, Germany

Edited by David A. Weitz, Harvard University, Cambridge, MA, and approved November 25, 2019 (received for review May 7, 2019)

Dendritic cells “patrol” the human body to detect pathogens. In their search, dendritic cells perform a random walk by amoeboid migration. The efficiency of pathogen detection depends on the properties of the random walk. It is not known how the dendritic cells control these properties. Here, we quantify dendritic cell migration under well-defined 2-dimensional confinement and in a 3-dimensional collagen matrix through recording their long-term trajectories. We find 2 different migration states: persistent migration, during which the dendritic cells move along curved paths, and diffusive migration, which is characterized by successive sharp turns. These states exhibit differences in the actin distributions. Our theoretical and experimental analyses indicate that this kind of motion can be generated by spontaneous actin polymerization waves that contribute to dendritic cell polarization and migration. The relative distributions of persistent and diffusive migration can be changed by modification of the molecular actin filament nucleation and assembly rates. Thus, dendritic cells can control their migration patterns and adapt to specific environments. Our study offers an additional perspective on how dendritic cells tune their searches for pathogens.

amoeboid migration | dendritic cells | random cell trajectories | actin waves | Arp2/3

Cell migration is essential for biological processes, including embryogenesis, wound healing, and immune responses. In the absence of external cues, cells typically move randomly (1–4): for instance, to search for food or pathogens as is the case for immune cells that “patrol” an organism. The efficiency of searching by a cell depends on the characteristics of its random walk. In the presence of external cues, it is commonly assumed that the inherent random motion of cells is stabilized to more directional motion (5). In particular, chemical gradients guide cells to migrate toward food sources and sites of inflammation and away from potentially harmful substances.

A well-studied example is the bacterium *Escherichia coli*, which moves in a sequence of directional runs and reorienting tumbles (6). The bacterium is propelled by a bundle of flagella that rotate counterclockwise. When a sufficient number of the flagella rotate clockwise, the bundle opens up, which leads to tumbling (6, 7). Changes in the concentrations of certain substances can either lengthen or shorten the run phases, which depends on whether the bacterium is swimming in a favorable direction or not.

In contrast, it is less well known how the erratic migration patterns of animal cells that move on substrates or in 3-dimensional (3D) porous environments are determined (5, 8, 9). A common motif of actin-driven migration consists of the actin filament assembly that drives the formation of a protrusion, which thus defines the leading edge of the cell (8). In addition, myosin-induced contraction pulls the cell body forward and simultaneously generates retrograde actin flow away from the leading edge (10–12). Directionality

of cell migration can be changed by alterations of the actin cytoskeleton either gradually or by completely depolarizing the cell.

There are several possibilities for how an animal cell might regulate its random motion to adapt its search strategy to its environment. For example, cells can exploit polarity cues in the form of adhesion or interactions with microtubules to stabilize the actin dynamics at the leading edge (13–15). Furthermore, there is positive feedback between the speed of myosin-driven retrograde flow and the cell persistence (16). Another possibility has been suggested to involve actin polymerization waves that are now recognized as part of the organization of the actin network in a large number of cell types (17–19) and that are known to be associated with phagocytosis and cell migration (20, 21). Theoretical analysis has shown that such waves can generate migration patterns even in the absence of molecular noise (22), including random migration patterns (23).

In this study, we investigated the migration of immature dendritic cells (DCs), which show amoeboid motion when strictly confined. This motion is independent of adhesion molecules (24) and microtubules (25), but it relies on actin polymerization and actomyosin contractility (26). We show that DC trajectories can be divided in persistent and diffusive segments, during which the cells

Significance

Dendritic cells are immune cells that migrate within the human body in search of pathogens. This search is performed by a random walk, which combines persistent and diffuse movements. The mechanism underlying this random walk is currently not known. We analyzed very long trajectories of dendritic cells *ex vivo*, and we describe here their characteristic persistent and diffusive patterns. Together with theoretical analysis, we provide evidence that the random walk of dendritic cells could be a consequence of the intrinsic actin dynamics without need for molecular noise or external polarization cues. Our results hint at the possibility that these cells can adapt their random search strategies by changing the spontaneous dynamics of their actin cytoskeleton.

Author contributions: L.S., N.E., K.K., and F.L. designed research; L.S., N.E., E.T., and R.S. performed research; P.M., P.V., A.-M.L.-D., M.P., B.Q., and M.H. contributed new reagents/analytic tools; L.S., N.E., E.T., R.S., K.K., and F.L. analyzed data; and L.S., N.E., K.K., and F.L. wrote the paper.

The authors declare no competing interest.

This article is a PNAS Direct Submission.

Published under the PNAS license.

¹L.S. and N.E. contributed equally to this work.

²To whom correspondence may be addressed. Email: f.lautenschlaeger@physik.uni-saarland.de.

This article contains supporting information online at <https://www.pnas.org/lookup/suppl/doi:10.1073/pnas.1907845117/-DCSupplemental>.

First published December 27, 2019.

move in curves or fluctuate on the spot. We relate this behavior to the dynamics of the actin network and show theoretically that this can result from spontaneous actin polymerization waves. Indeed, we observed spiral actin polymerization waves that are compatible with these theoretical predictions. Our study provides evidence that the intrinsic assembly dynamics of the actin cytoskeleton generate polarity cues and determine the persistence of DC migration.

Results and Discussion

Immature DCs Can Show Two Distinct States of Migration. To investigate the searching strategies used by immature DCs, we used primary mouse immature DCs derived from bone marrow of Lifect-GFP knock-in mice. We visualized DC migration at 37 °C confined between the cell culture dish and a “roof” that was held by microfabricated pillars. In these environments, the cells moved essentially freely and without the need to adhere to a substrate (27) (Fig. 1A). The culture dish and the confining roof surfaces

were coated with a nonadhesive random graft copolymer with a poly(L-lysine) backbone and poly(ethylene glycol) side chains to exclude movement by cell adhesion. The cells were imaged every 3 min using phase contrast microscopy, and their Hoechst-stained nuclei were tracked using epifluorescence microscopy (*Materials and Methods*). The trajectories of migrating DCs were recorded for 5 to 15 h, during which time the cells typically moved for a total distance of 250 μm , which corresponds to ~ 12 cell diameters. In the absence of external directional cues, the DCs switched between a persistent and a diffusive migration mode. During persistent migration, DCs move along a curved trajectory for extended time intervals, while the diffusive motion is defined as a pause in forward movement for a certain time interval, during which the DCs fluctuate around their specific location (Fig. 1B and C and *Movies S1–S3*).

For quantitative analysis of these 2 migration modes, we introduced a formal definition. This was based on identifying diffusive segments, whereby the nondiffusive segments were classified as persistent. The diffusive state was defined by the trajectory of the center of mass of the cell nucleus presenting sudden changes of the direction of motion. Specifically, we considered the displacement vectors from one frame to the next. The “turning angle” was defined as the angle between 2 consecutive displacement vectors. A change in direction is “abrupt” for a turning angle $> 90^\circ$. A 12-min segment of the trajectory was classified as diffusive if it contained at least 2 abrupt directional changes. As judged by visual inspection, this criterion gave good segmentation of the trajectories into persistent and diffusive segments (Fig. 1C).

The single DCs spent $56 \pm 37\%$ of the time migrating persistently and $44 \pm 37\%$ of the time diffusing along their trajectories. The full range of the data obtained here is given in *SI Appendix, Tables S1–S3*. The times that the DCs remained in each of these states were exponentially distributed, with switching rates of 4.7 and 4.4 h^{-1} , respectively. This corresponds to characteristic times of 12.8 min spent in the persistent and 13.7 min spent in the diffusive state (*SI Appendix, Fig. S1D and E*). In determining these quantities, only those segments that started and ended during the observation period were considered. On this basis, 28% of cells that showed only persistent migration (*SI Appendix, Fig. S1A*) were not taken into account. The time that these DCs spent in the persistent state would actually be longer, but it cannot be measured accurately as there were no clearly defined end points.

The instantaneous cell speed was obtained by dividing the DC displacement between 2 video frames by the corresponding time difference. During persistent migration, the DCs moved significantly faster ($5.5 \pm 3.4 \mu\text{m min}^{-1}$) than during diffusive migration ($3.1 \pm 2.7 \mu\text{m min}^{-1}$; $P < 0.0001$) (*Materials and Methods*), which led to an overall mean speed of $4.3 \pm 3.2 \mu\text{m min}^{-1}$ (Fig. 1D and *SI Appendix, Table S2*). The distribution of the turning angles had a pronounced peak at 0° in the persistent state, whereas it was nearly uniform in the diffusive state (Fig. 1E). This symmetric distribution of the turning angles around 0° shows that there was no preferred “handedness” of the curved segments. The curvature of the trajectories was measured by locally fitting circles (Fig. 1F and *Materials and Methods*), which was possible along 36.9% of the trajectories (52.1% along persistent segments; 28.9% along diffusive segments; including the fitted mixed segments) (*Materials and Methods*). The distribution of the radii obtained here from the analysis of 2,538 trajectories showed an overall mean of $60.7 \pm 58.3 \mu\text{m}$ (77.9 μm for persistent segments; 27.7 μm for diffusive segments; 54.1 μm for mixed segments) (Fig. 1F and *SI Appendix, Table S3*). Overall, the most frequent radius was 31.9 μm (46.7, 15.0, and 29.4 μm for persistent, diffusive, and mixed segments). For the large radii, the distribution decayed exponentially with a characteristic length of 41.0 μm .

We could not detect any correlations between the direction of motion immediately before and immediately after diffusive segments (*SI Appendix, Fig. S2*), and the distribution of the relative angle between the directions of motion before and after diffusive

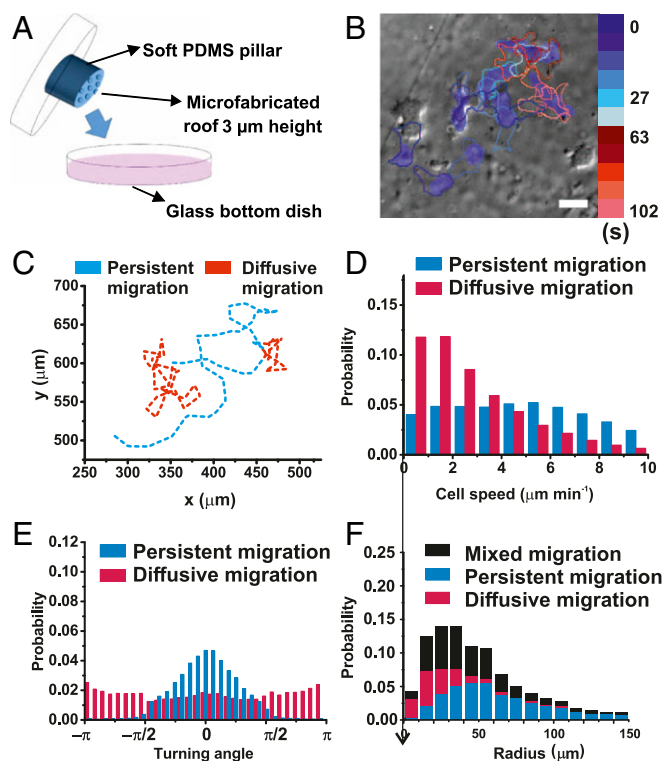


Fig. 1. Immature DCs switch between persistent and diffusive states during migration. (A) Scheme of a microfabricated roof used to confine cells during migration experiments. Microfabricated roof was assembled according to ref. 27 and consists of a soft pillar of the silicon-based organic polymer polydimethylsiloxane (PDMS) attached to the lid of a cell culture dish to give support to the glass coverslip coated with PDMS micropillars of 3- μm height and 1-mm spacing. When the dish is closed, the soft PDMS pillar is slightly compressed while keeping the 3- μm pillars in contact with the bottom of the culture dish. (B) Representative images of DC trajectories. Images were acquired at 3-min time points. Hoechst-stained nuclei are colored in blue. (C) Characterization of DC trajectories of tracked nuclei by fitting circles to the segments of the trajectories. (D) Distribution of migration speeds of immature migrating DCs in the persistent (blue) and diffusive (magenta) states. Mean speed during persistent migration was $5.5 \pm 3.3 \mu\text{m min}^{-1}$ (SD), and during diffusive, migration was $3.1 \pm 2.7 \mu\text{m min}^{-1}$ (SD). (E) Distribution of turning angles in the persistent (blue) and diffusive (magenta) states. (F) Radii of curvature for DCs migrating under confinement for persistent (blue), diffusive (magenta), and mixed (black) segments of trajectories. Analysis included 9,460 radii from 2,538 trajectories. Most frequent radius, $R_{\text{typ}} = 31.6 \mu\text{m}$.

migration was uniform (*SI Appendix, Fig. S2*). Also, the handedness of the trajectory before and after diffusive migration was not correlated (*SI Appendix, Fig. S2B*).

DC Migration in 3D Collagen Gels Also Shows Persistent and Diffusive Migration. To determine whether persistent and diffusive migrations were specific to the quasi-2-dimensional (quasi-2D) roof geometry, DCs were also tracked in a 3D collagen matrix. Pepsin-extracted bovine hide collagen type I (part Type III; Advanced Biomatrix; Nutragen) was used for this matrix preparation. After polymerization at 37 °C, this collagen formulation produces homogenous matrices with pore sizes in the lower micrometer range. The collagen was mixed with the cell solution to a final concentration of 2.5 mg mL⁻¹.

When the DCs were imaged in the collagen matrix using selected plane illumination microscopy, a similar pattern of persistent and diffusive migration was seen as in the quasi-2D roof geometry (*SI Appendix, Fig. S3A* and *Movie S4*). During persistent migration, the mean radius of curvature of the 3D trajectories was $29.7 \pm 14.9 \mu\text{m}$ (*SI Appendix, Fig. S3D* and *Table S3*) and was thus smaller than for the quasi-2D case. The DCs spent a mean of $62 \pm 29\%$ of the time in persistent migration and the remaining $38 \pm 29\%$ of the time in diffusive migration (*SI Appendix, Table S1*). The overall mean migration speed was $1.6 \pm 2.0 \mu\text{m min}^{-1}$ ($2.3 \pm 1.6 \mu\text{m min}^{-1}$ during persistent migration; $1.0 \pm 1.2 \mu\text{m min}^{-1}$ during diffusive migration) (*SI Appendix, Fig. S3B* and *Table S2*) and thus, slower than for the quasi-2D roof geometry. The differences between the quasi-2D roof geometry and the 3D collagen network might arise from a higher degree of confinement and a more convoluted confinement geometry for the 3D network (28). We can conclude here that the persistent and diffusive migration of these DCs is not specific to any particular confinement geometry. On this basis and as the quantification of the motion in 2D is an easier task than for the 3D network, the rest of the study was performed using the quasi-2D roof geometry.

Immature DCs Perform Modified Persistent Random Walks. Important characteristics of the migration of several cell types can be captured by effective random walk processes (4). In particular, various models for persistent random walks, where the walker has a finite memory of his direction of motion, and active Brownian particles, which move at a constant speed and for which the direction of motion fluctuates stochastically, have been used to this end. We have checked whether the persistent and diffusive migration of DCs is accounted for by standard random walks (*SI Appendix, Figs. S4 A, D, and G* and *S5 A, D, and G* and *Table S1*). For this, we simulated several standard random walkers (*Materials and Methods*) and applied the same analysis as above to the trajectories obtained in this way. The closest match to the experimental data that we could get was through a modified persistent random walk or run and tumble, where during a period of straight motion, a random fluctuation of the direction of motion is selected uniformly from the interval $[-30^\circ, 30^\circ]$ around the straight path (*SI Appendix, Fig. S4 G-I*). The lengths of straight segments were distributed exponentially. The distribution of the radii of curvature was in good agreement with the experimental values. Note, however, that the distribution of these radii of curvature depends in a sensitive manner on the sampling rate.

Actin Nucleation and Contraction Affect Persistent and Diffusive Migration. Migration of DCs is a result of protrusions that are generated by actin polymerization in connection with myosin-induced contraction (29). To determine whether actin polymerization is involved in persistent and diffusive migration, we interfered with these processes by applying various inhibitors.

The Arp2/3 complex nucleates new actin filaments by promoting their branching off from existing filaments (30, 31). After treating the DCs with the Arp2/3 nucleation inhibitor CK666 (50,

100 μM), they survived similarly to the controls over the next 18 h (*SI Appendix, Fig. S6*). Under this condition, there was a significant increase in the proportion of time spent diffusing (control, 44%; 100 μM CK666, 62%, $P < 0.0001$; 150 μM CK666, 66%, $P < 0.0001$) (*Fig. 2A* and *SI Appendix, Fig. S7A*). In contrast, CK666 treatment did not significantly change the mean cell speeds for persistent and diffusive migration (*SI Appendix, Table S2*), the distributions of turning angles in either state (*Fig. 2B*), or the distribution of the radii of curvature (*Fig. 2C* and *SI Appendix, Table S3*).

Formins constitute a second major family of actin nucleators (32, 33) that also promote filament elongation (34) and generate longer filaments than Arp2/3 (35). Application of the inhibitor of the formin domain FH2, SMIFH2 (12.5 μM) (36), did not have any significant effects on the relative duration of time spent in the persistent and diffusive states of these DCs (*Fig. 2D* and *E* and *SI Appendix, Fig. S5A*). However, this formin inhibition significantly increased the mean speed in both states to $7.2 \pm 4.0 \mu\text{m min}^{-1}$ for persistent and $4.1 \pm 3.3 \mu\text{m min}^{-1}$ for diffusive migration ($P < 0.0001$). At the higher concentration of 25 μM SMIFH2, these mean speeds were the same as for the untreated control DCs (*SI Appendix, Fig. S8*), although 60% of the cells died after 18 h (*SI Appendix, Fig. S6B*); therefore, 12.5 μM SMIFH2 was used for further experiments. The distribution of the turning angles did not change significantly with 12.5 μM SMIFH2 (*Fig. 2E*), but in the persistent state, the mean radius of curvature increased to $107.4 \pm 128.3 \mu\text{m}$ (*Fig. 2F* and *SI Appendix, Table S3*).

Finally, the activity of myosin was inhibited by treatment with the Rho-associated protein kinase (ROCK) inhibitor Y27632 (30 μM), which also affects actin filament assembly (37, 38). Here, the fraction of time spent in persistent migration increased to 79%. At the same time, the mean speed decreased to $3.1 \pm 2.0 \mu\text{m min}^{-1}$ for persistent and $1.7 \pm 1.8 \mu\text{m min}^{-1}$ for diffusive migration (*Fig. 2G*). The distribution of the turning angles during persistent migration also narrowed significantly, with an SD of 0.67 rad compared with 0.83 rad in the control (*Figs. 1E* and *2H*). However, the distribution of the radii of curvature was very similar to the control (*Fig. 2I*).

For all of these inhibitor treatments, the overall mean cell speed changed significantly compared with the control (*Fig. 2J*, $P < 0.0001$, and *SI Appendix, Table S2*). Also, the persistence length, which measures how quickly the direction of migration change was modified by each of these 3 inhibitors (*Fig. 2K*), decreased significantly with CK666 and SMIFH2 but increased significantly with Y27632. The typical radius of curvature was little affected by these inhibitors (*Fig. 2L* and *SI Appendix, Table S3*). On the basis of these data, we can conclude that the persistent state depends dominantly on Arp2/3 activity, whereas formin and myosin (ROCK) activity has larger effects on diffusive migration and/or cell speed than on persistent migration.

Cell Shapes Are More Stable during Persistent than during Diffusive Migration. To determine other measures that can be used to distinguish between the persistent and diffusive states, we analyzed the cell shape. We expected that shape changes occur on slower timescales during persistent than during diffusive migration. We tracked single DCs with higher spatial and temporal resolution than for the earlier experiments, with 5 s between frames, and for up to 68 min (*Movies S5* and *S6*). From these tracks, we obtained the average cell shapes in the direction of motion (*Materials and Methods*). For the control condition, these shapes were elongated during persistent migration, while they were nearly circular during diffusion (*Fig. 3A* and *B* and *Movies S7-S9*). This was also seen for the cells treated with the Arp2/3, formin, and ROCK inhibitors (*SI Appendix, Fig. S9* and *Movies S10-S15*). To quantify this difference, which would give us an alternative method to define persistent and diffusive migration, we considered the shapes' Fourier spectra. Despite the apparent differences during persistent and diffusive migration, their Fourier

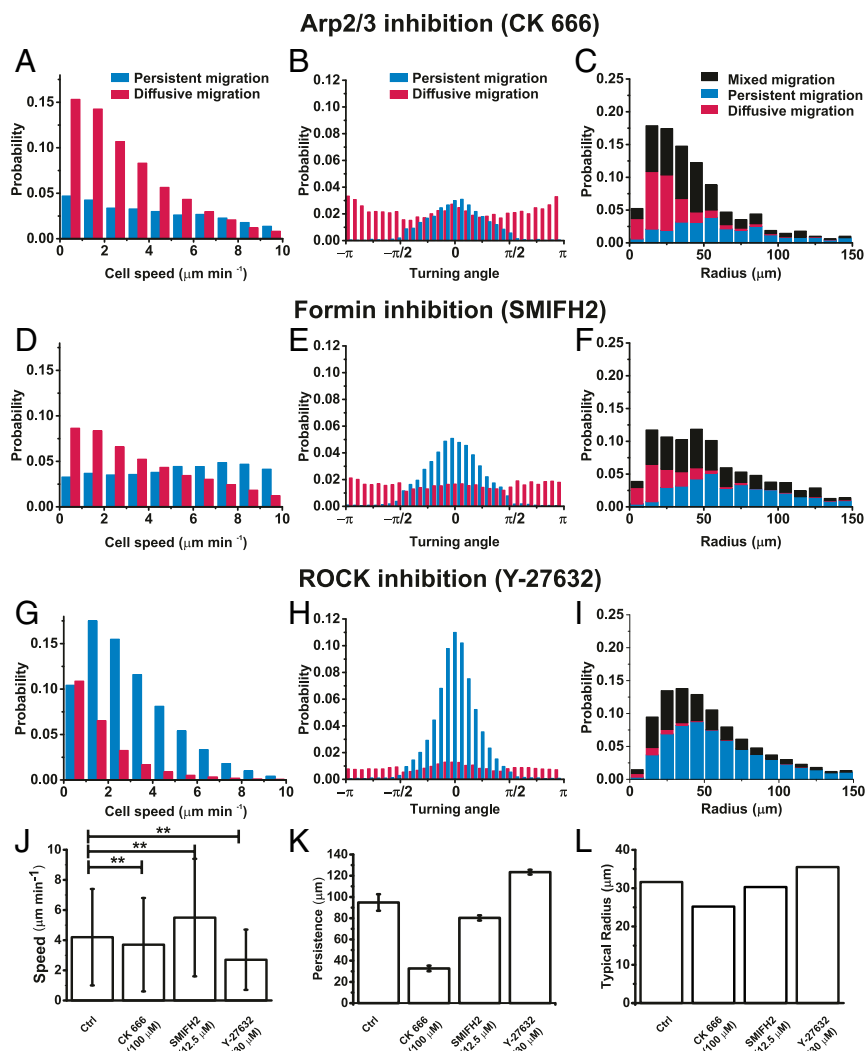


Fig. 2. Actin polymerization affects immature DC migration. (A–I) Distributions of migration speeds (A, D, and G), turning angles (B, E, and H), and radii of curvature (C, F, and I) after treatments with 100 μM CK 666 (A–C; Arp2/3 inhibition), 12.5 μM SMIFH2 (D–F; formin inhibition), and 30 μM Y-27632 (G–I; ROCK inhibition) for DCs migrating under confinement. We distinguish between persistent (blue), diffusive (magenta), and mixed (black; where indicated) segments of the trajectories. (J–L) Corresponding mean speed (J), persistence length (K), and typical radius of curvature (L) of complete datasets for the different conditions. Trajectories were acquired from at least 3 independent experiments. Number of analyzed trajectories: control (Ctrl): 1,752; CK666: 50 μM , 160; 100 μM , 271; 150 μM , 85; SMIFH2: 12.5 μM , 1,041; 25 μM , 298; Y27632: 30 μM , 1,635; 60 μM , 69. Data are means \pm SD. ** $P < 0.01$ (Mann–Whitney U and 2-sample t test).

spectra were not significantly different (Fig. 3 C and D). However, the autocorrelation function of the second Fourier mode's phase relaxed ≥ 5 -fold faster during diffusive than during persistent migration (Fig. 3E), which reflects that the cell shape changes faster in the former state. We used this criterion to distinguish between the 2 states in these shorter movies. By visual inspection, this agrees better with the form of the trajectories than the original criterion (Fig. 3F), where diffusive migration was characterized by at least 2 strong changes of the turning angles $> 90^\circ$ within 12-min segments of the trajectory.

Actin Localization Differs between Persistent and Diffusive States. To determine the role of actin for the persistent and diffusive states more directly, we measured its distribution in the migrating DCs at the high temporal and spatial resolutions we had used to analyze the cell shape. We used Lifeact-GFP as a fluorescent marker of filamentous actin (39). On the coarsest level of resolution using epifluorescence images, during persistent migration the fluorescence intensity was higher at the rear of the cells than

at the front (Fig. 4A, *SI Appendix*, Fig. S10, and *Movie S5*). In contrast, during diffusive migration, the fluorescence signal was more uniform throughout the cells, although patches of higher fluorescence intensity were often seen (Fig. 4B, *SI Appendix*, Fig. S10, and *Movie S6*).

We used particle image velocimetry to assess the dynamics of the actin distribution (Fig. 4C, $n = 377$ time points, and *Movies S7–S9*) (number of cells analyzed: 9). This method infers an apparent actin displacement field by aligning the actin distributions of 2 subsequent frames (*Materials and Methods*). During persistent migration, the mean apparent actin displacement field was mainly directed away from the leading edge but with a “sink” toward the trailing edge (Fig. 4C and *SI Appendix*, Fig. S10). The displacement field was symmetric with respect to the cell's direction of motion. This is in agreement with the accumulation of actin in the rear of the cell and compatible with a motor-induced retrograde flow (40). During diffusive migration, apparent actin displacements were directed radially outward at the cell boundary, whereas there was no coherent pattern in the cell interior (Fig. 4C

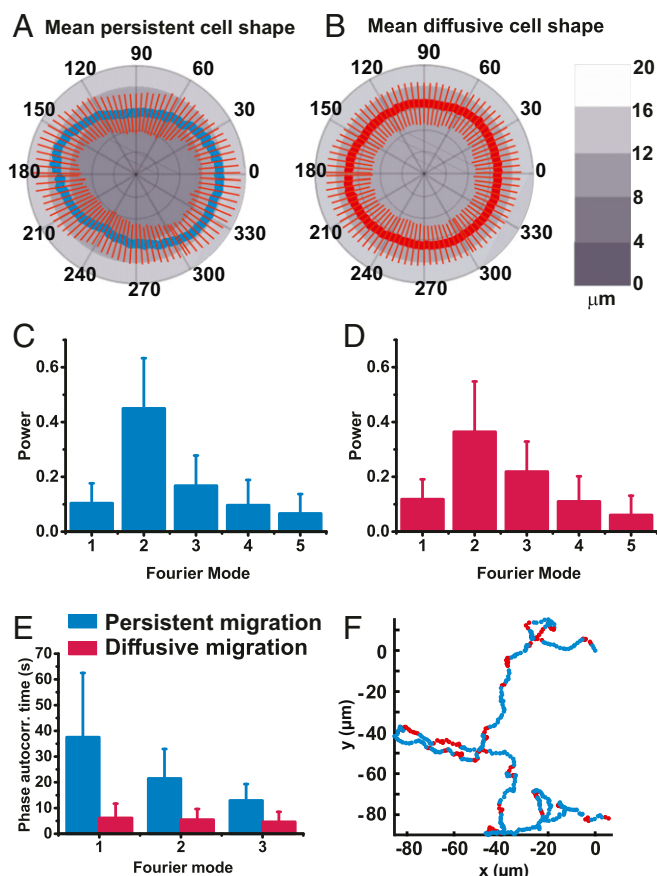


Fig. 3. Shape of confined migrating immature DCs differs in the persistent and the diffusive state. (A and B) Mean shapes of a representative control cell in its persistent (blue outline; averaged over $n = 109$ time points) and diffusive (red outline; averaged over $n = 267$ time points) states acquired as described in *Materials and Methods*. Direction of movement is toward 0° . Red bars indicate the SDs of the membrane segment position. (C and D) Mean Fourier power spectra of the first 5 Fourier modes of the shape for the same cell in the persistent (blue; C) and diffusive (red; D) states. (E) Fourier phase autocorrelation time for the first 3 Fourier modes acquired as described in *Materials and Methods*. (F) Trajectory of the same cell using the phase autocorrelation time to segment it into persistent (blue) and diffusive (red) states.

and *SI Appendix, Fig. S10*). On average, the distribution of apparent actin displacements at the boundary was isotropic. These displacements coincided with local expansions of the cell membrane (*Movie S9*), which is compatible with protrusions induced by actin polymerization.

We applied the same analysis to migrating DCs after inhibition of actin assembly or myosin activity (*SI Appendix, Fig. S11* and *Movies S10–S15*). With inhibition of the Arp2/3 complex using CK666, the cells appeared smaller compared with control cells (*SI Appendix, Fig. S11 A and B* and *Movies S10* and *S11*). In contrast, inhibition of formins using SMIFH2, if anything, increased the cell size (*SI Appendix, Fig. S11 C and D* and *Movies S12* and *S13*). In both cases, the average apparent displacement fields were similar to the corresponding fields in control cells. Inhibition of ROCK by applying Y27632 led to large fluctuations such that it was not possible to obtain a meaningful average actin displacement field (*Movies S14* and *S15*).

In summary, the average apparent actin displacement fields suggest that, compared with actin polymerization, myosin-induced actin flows are confined to regions away from the cell boundary and have only a small effect on changes in the direction of immature

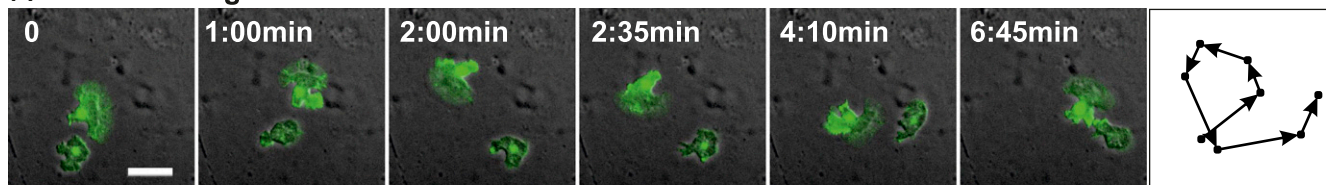
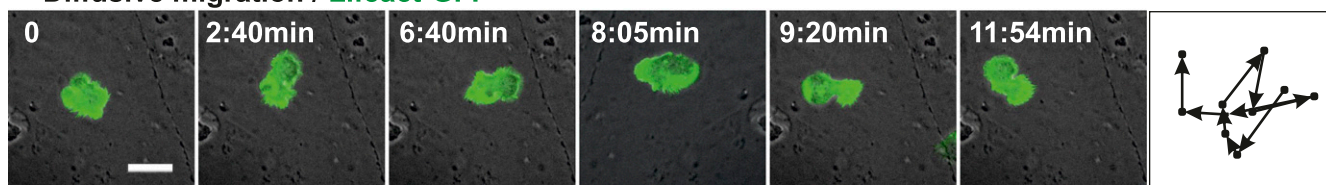
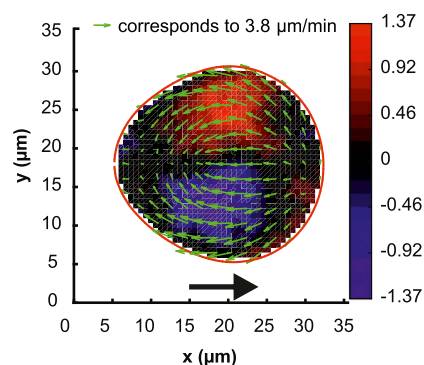
DC migration. This prompted us to theoretically investigate the role of the actin polymerization dynamics for the persistent and diffusive patterns.

A Deterministic Mechanism for Persistent and Diffusive Migration.

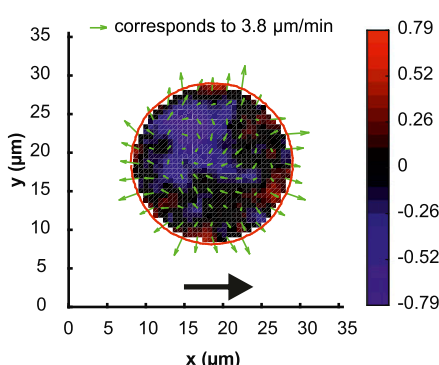
The switching between persistent and diffusive migration might result from amplification of molecular noise: as the assembly of filaments and the action of molecular motors are stochastic, the polarized organization of the actin cytoskeleton during persistent migration might be lost by chance. Diffusive migration would then correspond to the period until the spontaneous establishment of a new polarized state. In this case, an increase in the fraction of diffusive migration would be expected as the amount of filamentous actin was reduced. This is, however, at odds with our observations after the treatments with SMIFH2 (formin inhibition) and Y27632 (ROCK inhibition), which both led to reduced times spent in the diffusive state. We looked for a minimal mechanism for creating trajectories like the ones seen in the experiments. A candidate mechanism was suggested by a theoretical study showing that spontaneous actin polarization waves can generate, in the absence of molecular noise, distinct states of circular motion and of repolarization (23). We thus performed a theoretical analysis to see whether spontaneous actin polymerization waves can generate the persistent and diffusive migration of DCs.

As the molecular mechanism underlying actin waves is not yet known, we used a model of actin polymerization dynamics that omits molecular details (22). Actin polymerization waves show features that are expected for excitable systems. Along with a previous study (41, 42), we hypothesized that excitability results from excitatory interactions between actin nucleation factors. In our model, we assumed that inactive nucleators are activated spontaneously by binding to the plasma membrane, where co-operative effects increase the activation rates in the presence of active nucleators (Fig. 5A). Active nucleators generate actin filaments, which in turn, inactivate nucleators. We defined the model using a mean-field approach and described the system state in terms of the nucleator and filament distributions (*Materials and Methods*). The densities are coupled to the cell shape through a phase field. The system produced trajectories with alternating segments of circular motion and of repolarization that were reminiscent of the persistent and diffusive migration of the DCs (Fig. 5B and C, *SI Appendix, Fig. S12*, and *Movies S16* and *S17*). The parameter values chosen for the numerical solutions were in agreement with the experimental values whenever these were available (e.g., the speed and size of the cells). The other parameter values were chosen to obtain trajectories with similar characteristics to those of the DC trajectories (*Materials and Methods* and *SI Appendix, Table S4*).

We analyzed the computed trajectories using the same methods as for the cell trajectories indicated above. Similar to the DCs, the distribution of the radii of curvature of the computed trajectories decayed exponentially for larger radii with a characteristic length of $40.3 \mu\text{m}$ and did not show any difference for persistent migration in the clockwise or counterclockwise direction (Fig. 5C). The mean radius of curvature was $67.0 \pm 40.2 \mu\text{m}$ and showed good agreement with the experimental values together with the typical radii (*SI Appendix, Table S3*). The distribution of the turning angles peaked sharply around 0° in the persistent state but was much broader in the diffusive state (Fig. 5D), which mirrored the experimental data (Fig. 1D). For the computed trajectories, the mean speed during persistent migration was $4.5 \pm 0.7 \mu\text{m min}^{-1}$, whereas during diffusive migration, the mean speed was $3.1 \pm 1.4 \mu\text{m min}^{-1}$. Both of these mean speeds were similar to the experimental data (*SI Appendix, Table S2*). In the persistent segments of the computed trajectories, the distribution of the speeds was very narrow compared with the experimental distribution (Fig. 5E–G). Finally, here,

A Persistent migration / Lifeact-GFP**B Diffusive migration / Lifeact-GFP****C Persistent migration**

→ Migration direction
→ Actin displacement direction

Diffusive migration

Vorticity: ■ Counter clockwise
■ Clockwise

Fig. 4. Actin dynamics are different in the persistent and the diffusive state. Epifluorescence image sequences and trajectories (arrows; rightmost panel) of representative migrating Lifeact-GFP DCs in the persistent (A) and the diffusive (B) state. (Scale bar, 20 μm .) (C) Mean actin displacement field of a representative cell in the persistent and the diffusive state. Blue, clockwise vorticity; red, counterclockwise vorticity.

the computed trajectories showed persistent migration for 83% of the time, which was greater than that seen for the experimental data, and might reflect the absence of myosin-induced contractility in our theoretical description.

In the experimental system, we altered the actin dynamics through inhibition of actin nucleators. The inhibition of one nucleator should increase actin nucleation by the other. When increasing v_a in our model, we observed an increase in the fraction of time spent in the persistent state (Fig. 5 E–H). When lowering v_a , the speed distribution in the persistent states of the simulated trajectories remained the same, whereas the speed distribution in the diffusive state showed a shift of the mean speed from 3.5 to 2.1 $\mu\text{m min}^{-1}$. This suggests that the nucleator described in our model resembles Arp2/3 (SI Appendix, Fig. S8 A and D and Table S2).

Furthermore, when decreasing the total amount of nucleators, our numerical solutions of the dynamic equations showed a decrease of the wave amplitude and a weakened ability to deform the membrane. The simulated cells were slower and exhibited either circular or straight migration. For even lower nucleator abundance, the simulated cells did not polarize and were immobile. Increasing the amount of nucleators in our calculations increased the fraction of time spent in the diffusive state (SI Appendix, Table S5). These results indicate that lowering the activity or concentration of the nucleating protein hinders the cell's ability to (re-)polarize and reduces the mean speed.

On top of that, our analysis shows that spontaneous actin polymerization waves can generate trajectories that are similar to those of DCs, even in the absence of molecular noise, and especially are sufficient to create comparable circular paths (SI Appendix, Fig. S13). We thus experimentally investigated the role of actin waves in the DCs.

Spiral Actin Waves Can Exert Forces on the Cell Membrane and Contribute to Cell Movement and Polarization. Our measurements of the actin dynamics reported above did not reveal actin waves. However, typically these are confined to the vicinity of the plasma membrane (17). We used total internal reflection fluorescence (TIRF) microscopy to observe the dynamics of actin filaments close to the substrate in confined DCs expressing Lifeact-GFP. Time-lapse TIRF images were taken every 3 s for at least 30 min (Movie S18). We noticed actin waves in 19 of 22 cells observed. To rule out the possibility that these waves were due to fluctuations of the cell membrane adjacent to the substrate, surface reflection interface contrast (SRIC) microscopy was used, which captures interference patterns that arise from light reflected from the surface with light reflected from the cell (43, 44) (Movie S19). These interference patterns are extremely sensitive to the distance of the membrane to the substrate. Although the SRIC data revealed wave-like dynamics, these were distinct from the actin waves observed using TIRF

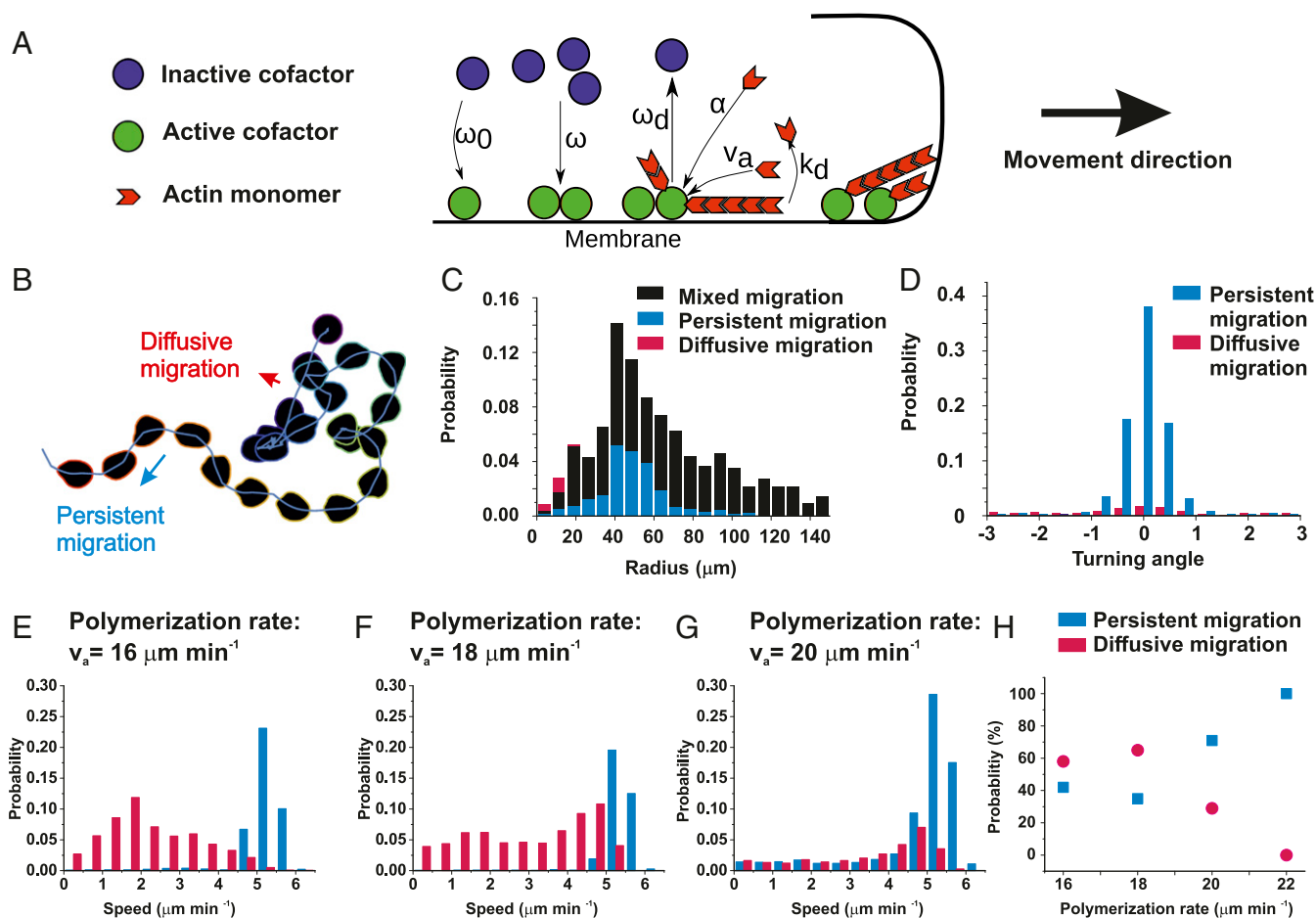


Fig. 5. Actin polymerization waves reproduce DC trajectories in theory. (A) Schematic view of the processes incorporated in the theoretical analysis (green circles, active nucleating proteins; blue circles, inactive nucleating proteins; red arrows, actin). (B) Example of a computed trajectory with cell shapes (black) shown at equidistant points in time. Both persistent and diffusive segments can be seen. (C) Distribution of radii of curvature for computed trajectories for persistent (blue) and mixed (black) segments. No circles could be fitted for diffusive segments. Data are from 24,337 radii from 10 computed trajectories. The mean radius is 67.0 μm . (D) Distribution of turning angles for computed persistent (blue) and diffusive (magenta) segments. (E–G) Distribution of migration speeds for computed persistent (blue) and diffusive (magenta) segments with distinct actin polymerization rates (v_a) as indicated. (H) Relative time spent in the persistent (blue) and the diffusive (magenta) states of computed trajectories in dependence on v_a . No changes for $v_a > 22 \mu\text{m}/\text{min}$.

microscopy (SI Appendix, Fig. S14). We therefore concluded that DCs show intracellular actin polymerization waves.

These actin polymerization waves either expanded isotropically or formed spirals until they encountered an obstacle or they died out spontaneously (Fig. 6A and B). When a wave reached the lateral boundary of a cell, displacement of the plasma membrane was detected (Fig. 6C). The mean speed of the advancing wave fronts varied from 9 to 11 $\mu\text{m min}^{-1}$ (Fig. 6D). These observations are compatible with the actin polymerization waves reported earlier (17, 19), and they show similar phenomenology to the waves obtained in the computations discussed above.

The direction of wave spreading was not confined to the direction of cell migration. Due to the high time resolution required for observing actin waves using TIRF microscopy, the cells suffered from photo damage after ~ 1 h. This experimental inconvenience meant that it was not possible to directly correlate the appearance and direction of actin polymerization waves with the persistent or diffusive migration as their detection required longer-term trajectories. Therefore, epifluorescence measurements were used, where actin wave patterns were also detected (Movies S6 and S8). The epifluorescence measurements allowed the correlation of cell direction and speed with actin protrusions at the cell edge (Fig. 4A and Movie S5). During diffusive migration, multiple actin waves emerged that pushed the cell membrane in

various directions and resulted in cell depolarization (Fig. 4B and Movie S6). Taken together, we can conclude that DCs show actin polymerization waves that can affect cell movement and alter the migration direction.

Spiral Actin Waves Are Arp2/3 Dependent. To gain further insight into the mechanisms involved in the generation of these actin polymerization waves, we analyzed the fraction of waves and their dynamics in DCs after treatments with the previously used inhibitors of Arp2/3, formins, and ROCK that are important for actin dynamics: CK666, SMIFH2, and Y27632 (Movies S20–S23). These treatments affected both the occurrence and dynamics of the actin polymerization waves (Fig. 7A–C). After all of these treatments, a smaller fraction of the DCs showed actin polymerization waves compared with the nontreated control DCs (Fig. 7D). Notably, significantly fewer DCs showed waves with CK666 treatment, which implied a central role of the Arp2/3 complex in actin wave formation (Movies S22 and S23). These data are in agreement with the alteration of the cellular trajectories after Arp2/3 treatment, which showed a large reduction in the fraction of cells in the persistent state compared with those in the diffusive state (Fig. 2B). When the formins were inhibited, the DCs still showed actin waves but with an increased frequency (Fig. 7B and E and Movie S21). As indicated above, the distributions of persistent and diffusive

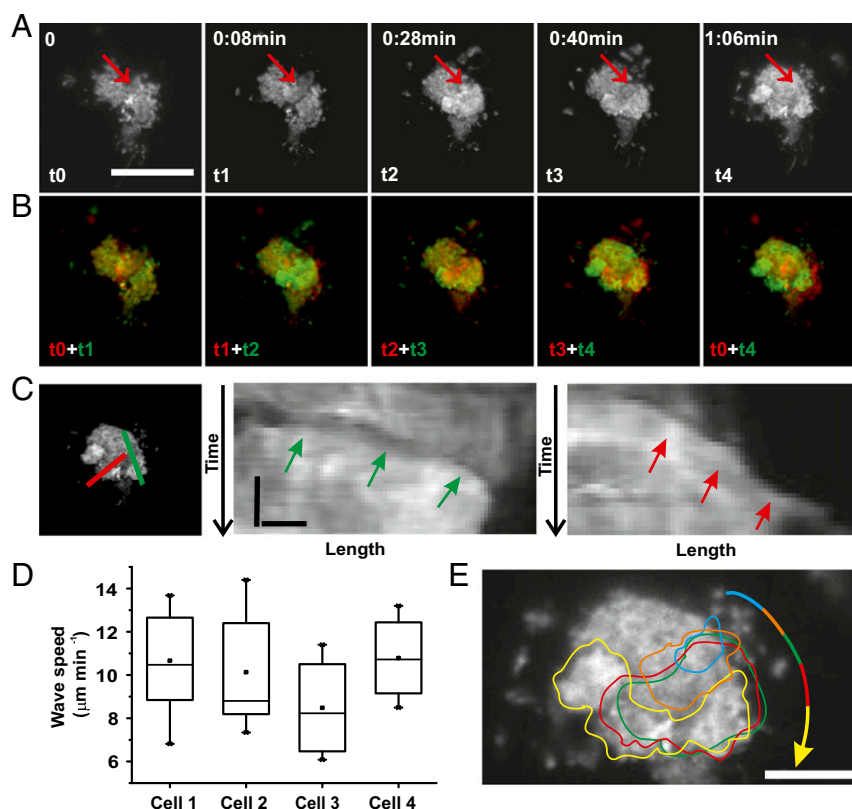


Fig. 6. Actin wave nucleation and propagation in migrating immature DCs. (A) Representative epifluorescence image sequences of actin wave formation and progression in an immature DC. Red arrows indicate origin of the wave. TIRF images of Lifeact-GFP were acquired every 2 s. (Scale bar, 20 μm .) (B) Overlay of cellular outline of 2 representative consecutive images displayed in A, illustrating the actin wave progression. Red indicates initial time t ; green indicates $t + 1$. The last image of the sequence is the overlay of t_0 (red) and t_4 (green). (C, Left) Representative wave analysis of wave from fluorescence TIRF images of Lifeact-GFP in the cell shown in A at t_4 . Red and green lines show the location along which the kymograph was generated (top left to bottom right). (C, Center and Right) Representative kymographs of wave propagation. Arrows indicate wave front. (Scale bars, 1 μm [length]; 10 s [time].) (D) Mean actin wave speeds obtained for 4 representative individual cells. Number of waves analyzed per cell: 11 (cell 1), 13 (cell 2), 4 (cell 3), and 8 (cell 4). Box plot displays mean speed (middle line) and SEM (box). (E) Contours of representative actin wave shown in A during propagation.

migration after formin inhibition were also similar to those of the control DCs (Fig. 2E). The ROCK inhibitor Y27632 did not significantly affect the frequency of actin wave formation (Fig. 7E and Movie S20). Finally, the actin wave propagation speed was significantly reduced after both formin and ROCK inhibition (Fig. 7F and Movies S20 and S21).

From the Arp2/3 inhibition data, we can conclude that Arp2/3 is required for the formation of the actin polymerization waves. This is also supported by the higher wave nucleation rate with formin inhibition, which would lead to more actin monomers available for Arp2/3-driven actin wave polymerization. We can further conclude that ROCK activity has little influence on actin wave generation but alters the wave propagation. These data are consistent with the effects of these inhibitors on the DC trajectories reported above (Fig. 2).

Conclusions

In this study, we confined immature DCs by 2 parallel slides to 2 dimensions, and we tracked them over several hours. The DCs performed random walks that were divided into 2 different states. In the persistent state, the DCs were polarized and moved continually along curved trajectories, with a mean radius of 61 μm . In the diffusive state, the DCs were not polarized, and they showed short irregular displacements. Biphasic migration patterns have been observed in several cell types before. When confined to 1-dimensional channels, DCs were shown to switch between moving and not moving states (45). The bacterium *E.*

coli switches between “runs” and “tumbles,” and fish keratocytes switch between continuous random walks and continuously turning states in which they move for an extended period of time in circles with a radius comparable with the cell size (46, 47). However, both the form of the trajectories and the mechanisms behind these biphasic behaviors are different (6, 7). Maiuri et al. (16) attributed the biphasic migration pattern of DCs to fluctuating “polarity cues” that determined the direction of the actin flow. This flow, in turn, was responsible for propelling the cells. The relative strength of the stochastic polarity cues and the actin flow then determined whether the cells moved continuously, diffusively, or in a biphasic manner. The origin of the polarity cues, however, remained unspecified. Together with our theoretical analysis, our experimental data show that polarity cues can be generated by the cytoskeleton in a process of self-organization.

Remarkably, self-organization leads to the emergence of intermittent waves, which suggests a possible deterministic origin of the random cell migration. In our theoretical description of the actin dynamics, many of the molecular details of the regulation of actin polymerization were not included to concentrate on its essential features. The main feature is negative feedback between actin filaments and actin nucleators, which is in agreement with previous studies (17, 48, 49). Indeed, interfering with Arp2/3 or formins had large effects on the actin polymerization waves. Inhibition of formins led to short-lived waves and a higher wave nucleation rate. In contrast, inhibition of Arp2/3 completely suppressed the formation of actin polymerization waves. However,

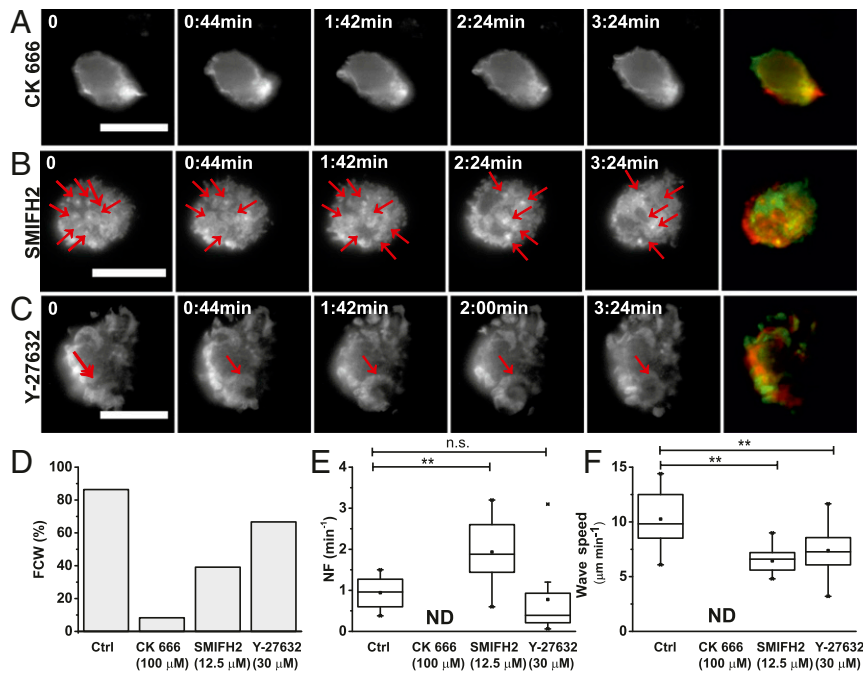


Fig. 7. Actin wave appearance is dependent on the Arp2/3 complex. (A–C) Representative time-lapse TIRF images after treatment with CK666 (A), SMIFH2 (B), and Y-27632 (C). Red arrows indicate origins of actin waves. Overlays show the first image of each sequence ($t = 0$ min; red) with the last image ($t = 3:24$ min; green). (Scale bars, 20 μm .) (D) Collected data showing fraction of cells with actin waves (FCW) following treatments. Control (Ctrl): 19 of 22 observed DCs showed waves; CK666: 1 of 12; SMIFH2: 9 of 23; Y27632: 6 of 9. (E and F) Mean nucleation frequency (NF; E) and speed (F) of actin waves following treatment. Box plots show means (middle lines) and SEMs (boxes). All cells were confined under 3 μm . ND, not determined; n.s., not significant. $**P \leq 0.01$ (2-sample t test).

these DCs continued to migrate. Indeed, similar to keratocytes, the migration of confined immature DCs depends on the action of the myosin motors (16, 29, 47). In our analysis, the effects of the myosin motors were not included as we focused on the directionality of the actin flow. Consequently, in our theoretical analysis, the cells were propelled by actin polymerization at the leading edge. In the future, it will be interesting to couple our wave generator to active gel theory to provide the full theory of actin-driven DC migration.

The observed migration pattern is known to have an important impact on cell search strategies (50). During diffusive migration, the DCs can search locally for pathogens and incorporate them via micropinocytosis (45), thus linking the nonmigrating state to cell function. Our study suggests that by changing specific parameters, such as the actin nucleation or polymerization rates, DCs can control essential features of their biphasic random walking. The dynamics inherent to the cytoskeleton and its ability to self-organize thus offer additional perspectives on how cells control their behavior.

Materials and Methods

Primary dendritic cells derived from the bone marrow (BMDs) of LifeAct-GFP mice were used in vitro to investigate amoeboid migration in 2D and 3D.

Breeding and humane killing of LifeAct-GFP mice are done in full conformity with 3R guidelines from Institut Curie Animal Welfare Body and European regulation in force. The 2D migration was observed in microfabricated roof chambers; 3D migration was in collagen gels. Cell trajectories were recorded by tracking Hoechst-stained cell nuclei in time-lapse images using custom-made software. The cell shape was obtained from image analysis of phase contrast images of BMDs. We extracted the cell's outline using custom-made software. Actin distributions were imaged using total internal reflection fluorescent microscopy.

In our theoretical analysis, we describe the state of the actin network in terms of its density T and its polarization \vec{p} . Their dynamics couple to the distributions n_a of active and n_i of inactive nucleators and to the phase field ψ . The dynamic equations are provided and explained in [SI Appendix](#) and were solved using spectral methods on Graphics Processing Units.

A detailed description of the materials and methods used in this work is in [SI Appendix](#).

Data Availability. All data discussed in the paper will be made available to readers on request.

ACKNOWLEDGMENTS. We thank Mael Leberre for discussing circular trajectories of DCs. We specifically thank the Saarland University and the Collaborative Research Centre 1027 funded by the German Science foundation (DFG) for funding. N.E. and K.K. further thank the Swiss National Science Foundation (grant 205321_175996) for financial support.

1. L. Li, S. F. Nørrelykke, E. C. Cox, Persistent cell motion in the absence of external signals: A search strategy for eukaryotic cells. *PLoS One* **3**, e2093 (2008).
2. M. H. Gail, C. W. Boone, The locomotion of mouse fibroblasts in tissue culture. *Biophys. J.* **10**, 980–993 (1970).
3. V. Tejedor, R. Voituriez, O. Bénichou, Optimizing persistent random searches. *Phys. Rev. Lett.* **108**, 088103 (2012).
4. D. Selmeczi et al., Cell motility as random motion: A review. *Eur. Phys. J. Spec. Top.* **157**, 1–15 (2008).
5. R. J. Petrie, A. D. Doyle, K. M. Yamada, Random versus directionally persistent cell migration. *Nat. Rev. Mol. Cell Biol.* **10**, 538–549 (2009).
6. H. C. Berg, *E. coli in Motion* (Springer, New York, NY, 2004).
7. H. C. Berg, The rotary motor of bacterial flagella. *Annu. Rev. Biochem.* **72**, 19–54 (2003).

8. B. R. Graziano, O. D. Weiner, Self-organization of protrusions and polarity during eukaryotic chemotaxis. *Curr. Opin. Cell Biol.* **30**, 60–67 (2014).
9. Y. Arai et al., Self-organization of the phosphatidylinositol lipids signaling system for random cell migration. *Proc. Natl. Acad. Sci. U.S.A.* **107**, 12399–12404 (2010).
10. F. Coussen, D. Choquet, M. P. Sheetz, H. P. Erickson, Trimers of the fibronectin cell adhesion domain localize to actin filament bundles and undergo rearward translocation. *J. Cell Sci.* **115**, 2581–2590 (2002).
11. C. Jurado, J. R. Hserrick, J. Lee, Slipping or gripping? Fluorescent speckle microscopy in fish keratocytes reveals two different mechanisms for generating a retrograde flow of actin. *Mol. Biol. Cell* **16**, 507–518 (2005).
12. K. Kruse, J. F. Joanny, F. Jülicher, J. Prost, Contractility and retrograde flow in lamellipodium motion. *Phys. Biol.* **3**, 130–137 (2006).

13. T. Wittmann, G. M. Bokoch, C. M. Waterman-Storer, Regulation of leading edge microtubule and actin dynamics downstream of Rac1. *J. Cell Biol.* **161**, 845–851 (2003).
14. M. Dogterom, G. H. Koenderink, Actin-microtubule crosstalk in cell biology. *Nat. Rev. Mol. Cell Biol.* **20**, 38–54 (2019).
15. B. P. Bouchet, A. Akhmanova, Microtubules in 3D cell motility. *J. Cell Sci.* **130**, 39–50 (2017).
16. P. Maiuri *et al.*, Actin flows mediate a universal coupling between cell speed and cell persistence. *Cell* **161**, 374–386 (2015).
17. O. D. Weiner, W. A. Marganski, L. F. Wu, S. J. Altschuler, M. W. Kirschner, An actin-based wave generator organizes cell motility. *PLoS Biol.* **5**, e221 (2007).
18. T. Killich *et al.*, The locomotion, shape and pseudopodial dynamics of unstimulated Dictyostelium cells are not random. *J. Cell Sci.* **106**, 1005–1013 (1993).
19. T. Bretschneider *et al.*, Dynamic actin patterns and Arp2/3 assembly at the substrate-attached surface of motile cells. *Curr. Biol.* **14**, 1–10 (2004).
20. G. Gerisch *et al.*, Self-organizing actin waves as planar phagocytic cup structures. *Cell Adhes. Migr.* **3**, 373–382 (2009).
21. N. Inagaki, H. Katsuno, Actin waves: Origin of cell polarization and migration? *Trends Cell Biol.* **27**, 515–526 (2017).
22. K. Doubrovinski, K. Kruse, Cell motility resulting from spontaneous polymerization waves. *Phys. Rev. Lett.* **107**, 258103 (2011).
23. A. Dreher, I. S. Aranson, K. Kruse, Spiral actin-polymerization waves can generate amoeboidal cell crawling. *New J. Phys.* **16**, 055007 (2014).
24. T. Lämmermann *et al.*, Rapid leukocyte migration by integrin-independent flowing and squeezing. *Nature* **453**, 51–55 (2008).
25. S. Etienne-Manneville, Microtubules in cell migration. *Annu. Rev. Cell Dev. Biol.* **29**, 471–499 (2013).
26. T. Lämmermann, M. Sixt, Mechanical modes of ‘amoeboid’ cell migration. *Curr. Opin. Cell Biol.* **21**, 636–644 (2009).
27. M. Le Berre, E. Zlotek-Zlotkiewicz, D. Bonazzi, F. Lautenschlaeger, M. Piel, Methods for two-dimensional cell confinement. *Methods Cell Biol.* **121**, 213–229 (2014).
28. N. R. Lang *et al.*, Estimating the 3D pore size distribution of biopolymer networks from directionally biased data. *Biophys. J.* **105**, 1967–1975 (2013).
29. A. C. Callan-Jones, R. Voituriez, Actin flows in cell migration: From locomotion and polarity to trajectories. *Curr. Opin. Cell Biol.* **38**, 12–17 (2016).
30. L. Blanchoin *et al.*, Direct observation of dendritic actin filament networks nucleated by Arp2/3 complex and WASP/Scar proteins. *Nature* **404**, 1007–1011 (2000).
31. K. J. Amann, T. D. Pollard, The Arp2/3 complex nucleates actin filament branches from the sides of pre-existing filaments. *Nat. Cell Biol.* **3**, 306–310 (2001).
32. S. H. Zigmond, Formin-induced nucleation of actin filaments. *Curr. Opin. Cell Biol.* **16**, 99–105 (2004).
33. D. Breitsprecher, B. L. Goode, Formins at a glance. *J. Cell Sci.* **126**, 1–7 (2013).
34. N. Courtemanche, Mechanisms of formin-mediated actin assembly and dynamics. *Biophys. Rev.* **10**, 1553–1569 (2018).
35. M. Fritzsche, C. Erlenkämper, E. Moeendarbary, G. Charras, K. Kruse, Actin kinetics shapes cortical network structure and mechanics. *Sci. Adv.* **2**, e1501337 (2016).
36. S. A. Rizvi *et al.*, Identification and characterization of a small molecule inhibitor of formin-mediated actin assembly. *Chem. Biol.* **16**, 1158–1168 (2009).
37. T. Ishizaki *et al.*, Pharmacological properties of Y-27632, a specific inhibitor of rho-associated kinases. *Mol. Pharmacol.* **57**, 976–983 (2000).
38. K. Watanabe *et al.*, A ROCK inhibitor permits survival of dissociated human embryonic stem cells. *Nat. Biotechnol.* **25**, 681–686 (2007).
39. J. Riedl *et al.*, Lifeact mice for studying F-actin dynamics. *Nat. Methods* **7**, 168–169 (2010).
40. M. L. Gardel, I. C. Schneider, Y. Aratyn-Schaus, C. M. Waterman, Mechanical integration of actin and adhesion dynamics in cell migration. *Annu. Rev. Cell Dev. Biol.* **26**, 315–333 (2010).
41. O. D. Weiner *et al.*, Hem-1 complexes are essential for Rac activation, actin polymerization, and myosin regulation during neutrophil chemotaxis. *PLoS Biol.* **4**, e38 (2006).
42. A. J. Davidson, W. Wood, Unravelling the actin cytoskeleton: A new competitive edge? *Trends Cell Biol.* **26**, 569–576 (2016).
43. A. S. Curtis, The Mechanism of Adhesion of Cells to Glass, A study by interference reflection microscopy. *J. Cell Biol.* **20**, 199–215 (1964).
44. O. Theodoly, S. Gabriele, M. P. Valignat, Influence of surface reflective properties on differential interference contrast microscopy. *Opt. Express* **16**, 4547–4558 (2008).
45. M. Chabaud *et al.*, Cell migration and antigen capture are antagonistic processes coupled by myosin II in dendritic cells. *Nat. Commun.* **6**, 7526 (2015).
46. E. Lauga, W. R. DiLuzio, G. M. Whitesides, H. A. Stone, Swimming in circles: Motion of bacteria near solid boundaries. *Biophys. J.* **90**, 400–412 (2006).
47. G. M. Allen *et al.*, Cell mechanics at the rear act to steer the direction of cell migration. *bioRxiv*:10.1101/443408 (15 October 2018).
48. K. Doubrovinski, K. Kruse, Cytoskeletal waves in the absence of molecular motors. *EPL* **83**, 18003 (2008).
49. S. Whitelam, T. Bretschneider, N. J. Burroughs, Transformation from spots to waves in a model of actin pattern formation. *Phys. Rev. Lett.* **102**, 198103 (2009).
50. O. Benichou *et al.*, Intermittent search strategies. *Rev. Mod. Phys.* **83**, 81–129 (2011).